Synthesis-Dependent Surface Acidity and Structure of $SrTiO_3$ Nanoparticles

Federico A. Rabuffetti, Peter C. Stair, and Kenneth R. Poeppelmeier*

Department of Chemistry, Northwestern University, Evanston, Illinois 60208

Received: February 25, 2010; Revised Manuscript Received: April 15, 2010

Chemisorption of pyridine and atmospheric CO_2 followed by means of visible Raman and DRIFT spectroscopy were employed to investigate the surface acidity and structure of as-prepared $SrTiO_3$ (STO) samples synthesized using three different approaches, solid-state reaction, molten salt, and sol-precipitation–hydrothermal treatment. Samples prepared via solid-state reaction consisted of irregularly shaped polycrystalline grains with a BET surface area of $\sim$2 m^2/g, whereas those obtained via molten salt synthesis and sol-precipitation–hydrothermal treatment were single-crystalline nanocubes with the {100} faces primarily exposed and BET surface areas of $\sim$10 and 20 m^2/g, respectively. Pyridine and atmospheric CO_2 chemisorption demonstrated that the differences in surface acidity between samples synthesized using different approaches are rather slight with a mixture of SrO-based and TiO-based terminations observed in all cases. In contrast, the typology of surface carbonate species arising from the reactive adsorption of atmospheric CO_2 varied significantly between samples, indicating the atomic structure of STO surfaces depends strongly on the synthetic method employed. The presence of coordinatively unsaturated Ti^{4+} acid centers and highly nucleophilic O^{2-} anions is particularly relevant in the perspective of employing morphology-controlled perovskite nanoparticles as supports in catalytic applications such as the oxidation of hydrocarbons.

1. Introduction

Strontium titanate, $SrTiO_3$ (STO), is an important material in the fields of electronics and catalysis. Owing to its large dielectric nonlinearity, temperature-dependent dielectric tunability, and low microwave losses, this material is an ideal candidate for microwave devices operating at cryogenic temperatures.[1,2] In addition, due to its simple structure and semiconducting character, STO has been employed as a model for mixed-metal oxide supports in catalytic reactions such as the partial and total oxidation of hydrocarbons,[3,4] photoassisted splitting of H_2O[5−8] for H_2 generation, and reduction of CO_2[9−11] for production of CH_4 and CH_3OH. Electronic and catalytic applications require ceramic materials with controlled chemical composition, morphology, and atomic structure at both the bulk and surface levels. With particular regard to the surface, these features strongly affect the sintering behavior of the material, thereby influencing the electrical properties of the ceramic body employed in electronic applications, whereas in the case of catalytic applications they directly determine the surface chemistry.

Critical in the perspective of achieving atomic-level control over the oxide surface composition and structure is the understanding of the influence of the synthetic approach on these features, especially if they are to be tailored by employing chemical methods. Although investigations of the surface acidity and structure of polycrystalline STO samples have been reported in the literature,[3,4,12,13] a systematic, comparative study that describes how these are modified upon changing the synthetic approach is lacking. Oxide nanoparticles of well-defined composition, crystallinity, and morphology, synthesized employing different approaches, constitute ideal substrates for such a study, which is the focus of the present work.

This paper is organized as follows. The first section focuses on the chemical, structural, and morphological characterization of the bulk structure of STO samples prepared following three different synthetic approaches. X-ray diffraction, spectroscopic, surface area, and thermogravimetric data are presented that complement those reported in a previous paper.[14] The second section is devoted to the characterization of the structure and assessment of the acidity of the surface of STO samples by means of adsorption of probe molecules followed by vibrational spectroscopy. Specifically, data from the reactive adsorption of atmospheric CO_2 and pyridine are presented and discussed in the context of previous investigations of the surface acidity and structure of STO. The implications of these findings for the use of STO nanoparticles as supports in catalytic processes such as the oxidation of hydrocarbons are discussed as well.

2. Experimental Section

2.1. Sample Preparation. ***2.1.1. $SrTiO_3$.*** Three different synthetic approaches were employed in the preparation of the STO samples studied in this work: solid state reaction (SSR), molten salt synthesis (MSS), and sol-precipitation–hydrothermal treatment (HTS). Experimental procedures identical to those described in a previous paper were followed[14] with the only exception of the preparation of HTS STO nanoparticles where the hydrothermal treatment step was conducted for 36 h instead of 24 h.

2.1.2. TiO_2. Commercial TiO_2 anatase (99.9%, Aldrich) was employed as a reference in surface acidity studies.

2.2. Bulk Structure Characterization. ***2.2.1. X-ray Diffraction Analysis.*** X-ray diffraction (XRD) patterns were collected in the 2θ range 20−80° using a Rigaku DMAX diffractometer in the Bragg−Brentano configuration operated at 20 mA and 40 kV. Cu Kα radiation (λ = 1.5418 Å) filtered with Ni was employed. The step size and collection time were 0.025° and 1 s per step, respectively.

2.2.2. Surface Area Measurements. Brunauer−Emmett−Teller (BET) surface areas were measured by N_2 adsorption at −196 °C using a Micromeritics ASAP 2010 analyzer (Mi-

* To whom correspondence should be addressed. Email: krp@northwestern.edu.

10.1021/jp101727c
Published on Web 05/20/2010

cromeritics Instrument Corp.). Samples were degassed overnight at 200 °C under vacuum prior to measurement.

2.2.3. Visible Raman Spectroscopy. Raman spectra were recorded under ambient conditions using a Horiba TRIAX 550 single grating spectrometer equipped with a liquid nitrogen-cooled CCD detector and an edge filter to remove the Rayleigh scattering. The 488.0 nm radiation from a Lexel 95 SHG Ar^+ laser (Cambridge Lasers Laboratories) was employed as the excitation source. The power at the sample level was 20 mW. An ellipsoidal mirror was used to collect and focus the scattered radiation into the spectrometer. Cyclohexane, acetonitrile, ethyl acetate, trichloroethylene, and 4-acetamidophenol were employed as frequency standards for calibration of Raman shifts. The absolute accuracy of Raman shifts is estimated to be ± 1 cm^{-1}.

2.2.4. Thermogravimetric Analysis. Thermogravimetric analyses (TGA) were performed on a thermogravimetric analyzer TA Q50 (TA Instruments) under a dry, high purity N_2 flow (80 mL/min). Samples were heated from 30 to 1000 °C at a rate of 15 °C/min, and held at 1000 °C for 1 h.

2.3. Surface Acidity and Structure Characterization. ***2.3.1. Atmospheric CO_2 Chemisorption.*** *Mid-Infrared Diffuse Reflectance Fourier Transform Spectroscopy.* Mid-infrared diffuse reflectance Fourier transform (DRIFT) spectroscopic studies were conducted on as-prepared and in situ and ex situ thermally treated STO samples. DRIFT spectra were recorded on a Thermo Nicolet Nexus 870 FTIR (Thermo Fisher Scientific Inc.) equipped with an environmental chamber that allows in situ experiments to be conducted. The chamber possesses a gas inlet port connected to a gas manifold system, as well as a water-cooled heating stage whose temperature is regulated by means of a variable temperature controller connected to a K-type thermocouple in contact with the sample. All the gases employed in surface spectroscopic characterization experiments were of ultrahigh purity grade and dried prior to contact with the sample by passing them through a moisture trap containing MnO (99%, Alfa Aesar) and molecular sieves (5 Å, Aldrich). A constant flow rate of 80 mL/min was employed in all experiments. The experimental sequence employed for collection of DRIFT spectra can be described as follows. First, the as-prepared STO sample under study was loaded into the chamber and purged with N_2 for 0.5 h; then, a first spectrum was collected. Subsequently, the sample was subjected to an in situ thermal treatment at 500 °C for 1 h under O_2; samples subjected to such a treatment will be thereafter referred to as pretreated. After cooling down to 25 °C, the chamber was purged with N_2 for 0.5 h; then, a second spectrum was collected. Finally, the sample resulting from thermogravimetric analysis, that is, ex situ thermal treatment at 1000 °C, was loaded into the chamber and purged with N_2 for 0.5 h; then, a third spectrum was collected. In all cases, 256 scans, a spectral resolution of 4 cm^{-1}, and KBr as the reference material were employed for collection of DRIFT spectra. Reference spectra were acquired under identical conditions to those of the samples.

2.3.2. Pyridine Chemisorption. *Visible Raman Spectroscopy.* The surface acidity of STO samples was assessed by means of pyridine chemisorption followed using visible Raman and DRIFT spectroscopies. For Raman experiments, a custom-made fluidized bed reactor was employed; this setup was described in detail in a previous paper.[15] An injection port was installed at the entrance of the reactor by adding a U-shaped tube connected to the gas inlet. The U-shaped tube has a septum through which liquids can be dosed into the gas stream; for Raman experiments, helium was used as the purging gas. As-prepared samples were first pressed into wafers and subsequently ground. The ground sample was then sieved and particles having sizes ranging from 170 to 250 μm were loaded into the reactor's sample holder. The reactor was purged for 0.5 h and then 100 μL of pyridine (99.9%, EMD Chemicals) were introduced in the gas stream by means of a microsyringe. The reactor was purged for a period of 3 h, after which no significant variations in the intensity of the vibrational bands were observed; a Raman spectrum was then collected (Py/as-prepared/sample). All the considerations made in the "Bulk Structure Characterization" section of this work regarding the scattering excitation source, collection of the scattered light, and calibration of Raman shifts also apply to pyridine chemisorption experiments described in this section.

Mid-Infrared Diffuse Reflectance Fourier Transform Spectroscopy. An environmental chamber identical to that described was employed for DRIFTS experiments. Both as-prepared and pretreated samples were investigated. As-prepared samples were loaded into the chamber and purged with N_2 for 0.5 h; then, a reference spectrum was collected. Pyridine was subsequently introduced into the chamber at 25 °C by flowing N_2 through a saturator containing liquid pyridine; a five-minute exposure to pyridine was found to be sufficient to achieve saturation coverage. The chamber was purged with N_2 for a period of 1 h, after which no significant changes in the intensity of the vibrational bands were detected; a sample spectrum was then collected (Py/as-prepared/sample). In the case of pretreated samples, as-prepared samples were loaded into the chamber and pretreated as described earlier in this work (500 °C, 1 h, O_2 80 mL/min). After cooling down to 25 °C, the chamber was purged with N_2 for 0.5 h and a reference spectrum was collected. At this point, the sample was exposed to pyridine for 5 min and subsequently purged with N_2 for 1 h; then, a first sample spectrum was collected (Py/pretreated/sample). Temperature was increased to 150 °C and held constant for 1 h, under N_2 flow; after cooling down to 25 °C, a second sample spectrum was collected (Py/150 °C/sample). Finally, temperature was increased to 300 °C and held constant for 1 h, under N_2 flow; after cooling down to 25 °C, a third sample spectrum was collected (Py/300 °C/sample). Spectra were acquired using 1024 scans and a spectral resolution of 4 cm^{-1}.

Quantification of Surface Lewis Acidity. The total number of Lewis acid sites present in HTS STO nanoparticles was estimated by means of thermogravimetric analysis of pyridine and ammonia chemisorption. A 10−15 mg sample of the as-prepared HTS STO powder was loaded in the platinum pan of a thermogravimetric analyzer TA Q50. The sample was pretreated as described earlier in this work (500 °C, 1 h, O_2 80 mL/min), cooled to 150 °C, and purged with N_2 (80 mL/min) for 0.5 h. Then, at 150 °C pyridine or ammonia was introduced into the TGA furnace; a N_2 flow through a saturator containing liquid pyridine was used for the former, whereas a 5% NH_3/N_2 mixture (Air Liquide) was employed for the latter. After saturation coverage was achieved, the adsorbate dose was discontinued and the TGA furnace purged with N_2 for at least 4 h until no further desorption was detected. Total surface Lewis acidity was determined from the weight gain and expressed on the basis of sample mass (micromoles of adsorbate/gram of STO) and surface area (molecules of adsorbate/surface area unit of STO).

3. Results and Discussion

3.1. Bulk Structure Characterization. ***3.1.1. X-ray Diffraction Analysis.*** X-ray diffraction patterns of the as-prepared STO powders are shown in Figure 1; the diffraction pattern of

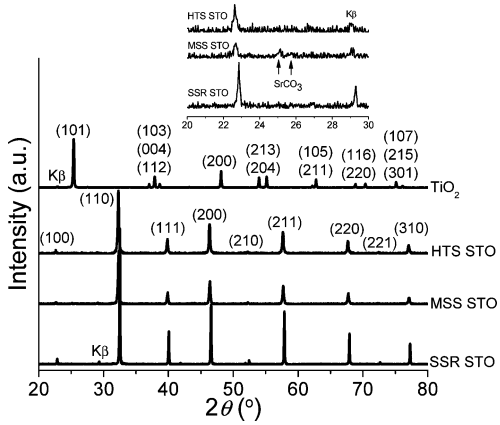

Figure 1. Powder X-ray diffraction patterns of SSR, MSS, HTS STO, and TiO_2. Inset: detailed view of the XRD patterns of SSR, MSS, and HTS STO in the 2θ range 20−30°, showing the presence of crystalline $SrCO_3$ in MSS STO.

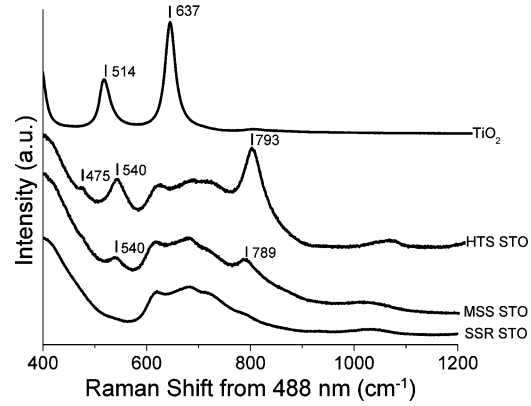

Figure 2. Raman spectra of SSR, MSS, and HTS STO, and TiO_2. First-order Raman peaks are denoted by their frequencies.

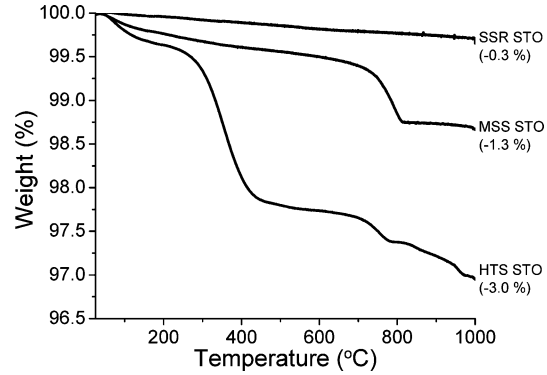

Figure 3. Thermograms of SSR, MSS, and HTS STO; the total weight loss is given in parentheses.

TiO_2 is displayed as well. SSR and HTS STO appear single phase to XRD, whereas MSS STO contains traces of $SrCO_3$ (PDF File No. 05-0418) as a secondary phase. For all three STO samples, all the diffraction maxima corresponding to the perovskite phase can be indexed to the cubic space group $Pm\bar{3}m$ with lattice constant $a \approx 3.90$ Å (PDF File No. 84-0444). The broadening of the peaks upon going from SSR to MSS and finally to HTS STO, reflects the decreasing size of the crystalline grains. In the case of TiO_2, the sample appears phase pure to XRD with all the diffraction maxima being matchable with the tetragonal space group $I4_1/amd$ (PDF File No. 21−1272).

3.1.2. Morphology and Surface Area. The morphological aspects of the STO samples studied in this work were described in detail in a previous paper.[14] Briefly, SSR STO consists of agglomerated, microcrystalline grains of average size ∼1 μm. MSS and HTS STO in turn, are single-crystalline, cubic-shaped nanoparticles of average sizes ∼120 and ∼60 nm, respectively, with the {100} faces primarily exposed. In these samples, interparticle agglomeration and sintering is greatly reduced with respect to SSR STO. In the case of HTS STO nanocubes, we reported the observation of a significant number of voids within the nanoparticle; a similar observation was reported by Hennings et al.[16] for $BaTiO_3$ (BTO) nanoparticles synthesized hydrothermally, and by Balaya et al.[17] for STO nanoparticles prepared via a peroxy-based route. Surface area measurements yielded values of ∼2, 10, and 20 m^2/g for SSR, MSS, and HTS STO, respectively, in excellent agreement with the calculated geometric surface area of the cubic shaped nanoparticles. This demonstrates that voids observed in HTS STO nanoparticles have a negligible contribution to the total surface area, that is, they are truly intragranular pores.

3.1.3. Visible Raman Spectroscopy. Raman spectra of the as-prepared STO samples are shown in Figure 2; the spectrum of TiO_2 has been included as well. The spectra of STO samples are dominated by two second-order broad bands at 600−800 and 950−1100 cm^{-1}, arising from additive combinations and overtones.[14,18−20] In addition to these features, the spectra of MSS and HTS STO nanoparticles display sharp peaks at 540 and ∼790 cm^{-1}, which are significantly more intense for the latter sample, which also displays an additional peak at 475 cm^{-1}. These sharp peaks are located at frequencies corresponding to those of single phonons[14] and, therefore, their presence demonstrates the activation of first-order Raman scattering in STO nanoparticles. At the origin of this phenomenon are local symmetry distortions, in particular the removal of the inversion symmetry, caused by a multiplicity of microstructural factors described in detail in a previous paper.[14]

The spectrum of TiO_2 anatase is in good agreement with previously reported spectra[21,22] and deserves no further considerations.

3.1.4. Thermogravimetric Analysis. Thermograms of the as-prepared STO powders are shown in Figure 3. SSR STO displays a total weight loss of ∼0.3% upon heating to 1000 °C. This weight loss is due to the removal of physisorbed and chemisorbed water, and decomposition of surface carbonate species resulting from the chemisorption of atmospheric CO_2; the nature of these species will be discussed in detail later in this work.

MSS STO in turn, exhibits a total weight loss of ∼1.3% that consists of a gradual weight loss from room temperature to 680 °C and a steep weight loss between 680 and 820 °C; these account for weight losses of ∼0.7 and ∼0.6%, respectively. The former weight loss is ascribed to the removal of physisorbed and chemisorbed water, whereas the latter corresponds to the decomposition of the $SrCO_3$ phase, in agreement with previous investigations of thermal decomposition of $SrCO_3$.[23−26]

HTS STO nanoparticles exhibit a total weight loss of ∼3.0%. Four contributions account for it, (1) An ∼0.3% weight loss between room temperature and 200 °C arising from the removal of physisorbed and weakly bound water. (2) An ∼2.0% broad weight loss between 200 and 600 °C mainly due to the removal of water incorporated within the bulk of the nanocrystal as OH groups[16,27−34] in situ DRIFT spectroscopy showed the dehydration of the surface contributes to this weight loss as well (see Supporting Information). (3) An ∼0.4% weight loss between 670 and 800 °C due to the decomposition of bulk $SrCO_3$ species not detected by XRD. (4) An ∼0.3% weight loss above 820 °C

TABLE 1: Chemical, Structural, and Morphological Characterization of the Bulk Structure of $SrTiO_3$ and TiO_2 Samples

sample	synthesis method	chemical composition[a]	symmetry	morphology[b]
SSR STO	solid-state reaction 1250 °C, 3.5 h, air	phase pure	$Pm\bar{3}m$ (XRD, Raman)	polycrystalline 1 μm, irregular shape 2 m^2/g
MSS STO	molten NaCl 820 °C, 3.5 h, Air	*P*: $SrTiO_3$ ($[V_{Sr}^{2+}] \approx 0.7\%$)[c] *S*: 0.6%[d] $SrCO_3$ (TGA, XRD, DRIFTS[e])	$Pm\bar{3}m$ (XRD, SAED[f]) with non-centrosymmetric domains (Raman)	single-crystalline 120 nm, cubic shape 10 m^2/g
HTS STO	sol-precipitation—hydrothermal treatment 240 °C, 36 h	*P*: $SrTiO_3$ ($[V_{Sr}^{2+}] = [V_{Ti}^{4+}] \approx 6.5\%$) *S*: ≈0.4% $SrCO_3$ (TGA, DRIFTS) *I*: ≈2% H_2O[g] (TGA)		single-crystalline 60 nm, cubic shape 20 m^2/g
TiO_2 (an.)	commercial	phase pure	$I4_1/amd$ (XRD, Raman)	10 m^2/g

[a] For samples containing more than one phase and/or bulk impurities, the following abbreviations are used: *P* = primary phase, *S* = secondary phase, and *I* = impurity. [b] See ref 14 for experimental morphological data other than the BET surface area. [c] Estimated concentrations of metal cation vacancies are given as molar percentage (per mol of STO). See text for details about their estimation. [d] Secondary phases and bulk impurities are given as weight percentages. [e] The experimental DRIFTS data is given in the "Surface Acidity and Structure Characterization" section of this work. [f] SAED: selected area electron diffraction. See ref 14. [g] Accounts for the total water content. See text for details.

arising from the densification of the nanoparticles via grain growth and reduction of the size of the intragranular pores.[16]

Results from thermogravimetric analysis demonstrate that the bulk microstructures of SSR, MSS, and HTS STO differ significantly from each other, in particular regarding the concentration of point defects present in the perovskite lattice. Indeed, according to these results, SSR STO has negligible cation vacancies, whereas MSS STO nanoparticles have ~0.7% (mol.) Sr^{2+} vacancies due to the segregation of 0.6% (w/w) of $SrCO_3$, which corresponds to a Sr-deficient powder with nominal formula $Sr_{0.993}TiO_{2.993}$. HTS STO nanoparticles in turn are expected to exhibit a significantly higher concentration of metal vacancies as a result of the incorporation of OH groups within the nanocrystal. To get a quantitative estimation of the metal cation vacancy concentration from thermogravimetric data, Hennings et al. developed a defect chemical model for BTO nanoparticles prepared under hydrothermal conditions.[16] In their model, the cation vacancies are fully ionized and equally distributed between the Sr and Ti sites. According to this model, the dehydration of the bulk of HTS STO nanoparticles can be described by the following reaction

$$[Sr_{1-x/6}(V_{Sr}^{2+})_{x/6}Ti_{1-x/6}(V_{Ti}^{4+})_{x/6}O_{3-x}(OH)_x] \rightarrow (1 - x/6)SrTiO_3 + (1/2)xH_2O$$

Ascribing the ~2.0% weight loss observed between 200 and 600 °C solely to the dehydration of the bulk, yields $Sr_{0.935}Ti_{0.935}O_{2.610}(OH)_{0.390}$ as the nominal formula for this sample. This corresponds to a vacancy concentration of ~6.5% (mol.) for Sr^{2+} and Ti^{4+}. These results are comparable to those of Hennings et al. who reported a vacancy concentration of ~7% (mol.) for each metal cation.[16] It is important to mention that these numbers likely constitute a slight overestimation of the actual cation vacancy concentration, because they were obtained under the assumption that the weight loss corresponds exclusively to the removal of bulk H_2O, that is, neglecting the contribution of the surface dehydration process.[29,34] Despite this fact, semiquantitative analysis of thermogravimetric data reported above shows a clear increase in the concentration of point defects present in the bulk of the perovskite lattice on going from SSR to MSS and finally to HTS STO. This observation, in conjunction with other microstructural features described in a previous paper,[14] correlates well with the magnitude of the local symmetry distortions observed in these samples using Raman spectroscopy.

Results on the characterization of the bulk structure of the samples studied in this work are summarized in Table 1.

3.2. Surface Acidity and Structure Characterization. ***3.2.1. Atmospheric CO_2 Chemisorption.*** *Mid-Infrared Diffuse Reflectance Fourier Transform Spectroscopy.* The presence and nature of surface species in the as-prepared STO samples, as well as the effect of the pretreatment on them, were investigated prior to pyridine chemisorption studies. DRIFT spectra of as-prepared STO samples are shown in Figure 4a−c in the 1200−1800 and 2400−2700 cm^{-1} regions; the spectrum of as-prepared TiO_2 in the 1200−1800 cm^{-1} region is also shown (Figure 4d). A variety of vibrational bands can be observed for STO each sample, owing to the presence of carbonate species arising from reaction with atmospheric CO_2. These carbonate species can be grouped into two categories: bulk and surface species. Bulk species consists of a $SrCO_3$ phase produced by the reaction of atmospheric CO_2 with SrO or $Sr(OH)_2$. Previous investigations of carbonate content in STO,[13,35] BTO,[36,37] and $(Ba,Sr)TiO_3$[38] polycrystalline samples reported that the following carbonate phase grains can be present: (1) as separate particles; (2) trapped into the bulk of the perovskite phase; or (3) on the surface of the perovskite grains. Surface species in turn arise from the reactive adsorption of atmospheric CO_2 on the oxide surface. Depending on the surface composition and atomic structure, as well as on the experimental conditions, several modes of adsorption of CO_2 are possible,[39−42] (1) adsorption on a metal cation, yielding a M−CO_2 complex in which the CO_2 molecule can exhibit linear or bent geometry; (2) monodentate carbonate, due to adsorption on an undercoordinated oxide ion; (3) bidentate carbonate, due to adsorption on an undercoordinated metal cation-oxide anion acid−base pair; (4) complex polydentate, bridging carbonate structures in which more than one metal cation-oxide anion pair is involved; and (5) bicarbonate, due to the reaction between a CO_2 molecule and a surface OH group. Carbonate species can be identified spectroscopically on the basis of the vibrational frequency of the double-degenerate, antisymmetric stretching mode of the carbonate ion.[43] This degeneracy is lifted upon placing the ion in a crystalline field[44−48] or upon coordination to the surface,[40,49−51] yielding two bands at specific frequency ranges in the 1200−1800 cm^{-1} region. The main spectroscopic features of bulk and surface carbonate species are summarized in Table 2; these,

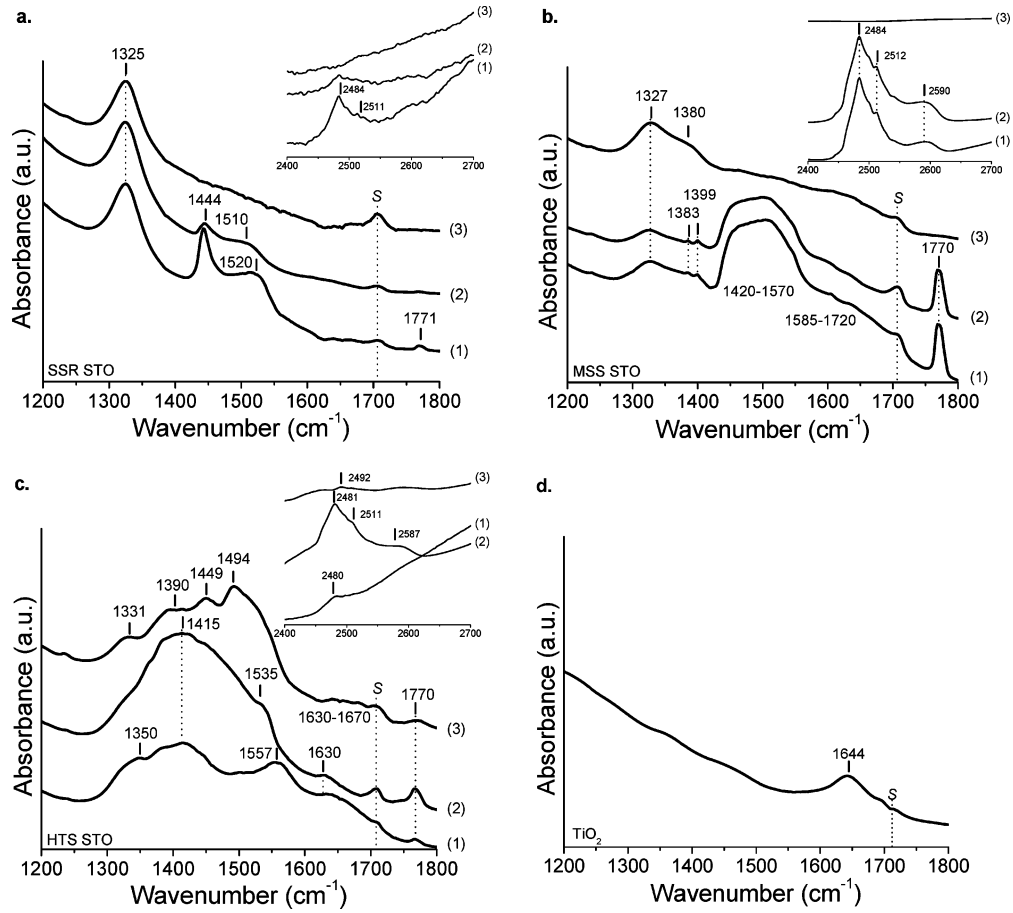

Figure 4. DRIFT spectra of (a) SSR STO, (b) MSS STO, (c) HTS STO, and (d) TiO_2. The following spectra are shown for each sample in the 1200−1800 and 2400−2700 cm^{-1} regions: (1) as-prepared, (2) in situ thermally treated at 500 °C for 1 h under O_2 flow, and (3) ex situ thermally treated at 1000 °C for 1 h under N_2 flow. Spectra were collected after loading the sample in the DRIFTS environmental cell, running the corresponding thermal treatment, and purging for 0.5 h with a high purity, dry N_2 flow. The peak labeled *S*, located at ∼1710 cm^{-1}, is an instrumental artifact.

TABLE 2: Infrared Vibrational Frequencies (in cm^{-1}) of Carbonate Species

	$\nu1$ (A_1')[a]	$\nu2$ (A_2')[a]	$\nu3$ (E′)[a]		$\nu4$ (E′)[a]		$\nu1+\nu3$		$\nu1+\nu4$
			Free CO_3^{2-} [b]						
	1063 (R)	879 (IR)	1415 (IR, R)		680 (IR, R)				
			Uncoordinated[c] CO_3^{2-} Species[d]						
	1020−1090	820−890	1420−1470		680−750				
			$SrCO_3$						
ref 45[e]	1075	860	1470[f]		699	707	2520		1795
ref 46[e]	1070	858	1453[f]		699	706			
ref 47[e]	1071	857	1471[f]		700	706	2484	2512	1771
ref 48	1074	857	1469	1531	699	706			
			Coordinated[g] CO_3^{2-} Species[d]						
monodentate	1040−1080	850−880	1300−1370	1470−1530	670−690	750−820			
bidentate	1020−1030	830−840	1260−1270	1590−1630	660−680	740−760			
bicarbonate	990−1050	830−840	1290−1410	1620−1660	698−705				

[a] Fundamentals modes of the free carbonate ion: $\nu1$ = symmetric stretch, $\nu2$ = out-of-plane deformation, $\nu3$ = asymmetric stretch, and $\nu4$ = in-plane deformation. The corresponding symmetry species are given in parentheses. [b] Ref 43. Selection rules: *R* = Raman active, and IR = infrared active. [c] Ionic carbonates. [d] Ref 51. [e] No splitting of the $\nu3$ mode was reported. [f] Broad band. [g] Cobalt(III) carbonato complexes.

along with thermal stability considerations, will be employed in this work to identify the nature of the carbonate species present in the as-prepared STO samples.

The DRIFT spectrum of as-prepared SSR STO (Figure 4a, spectrum (1)) displays two sharp and intense peaks at 1325 and 1444 cm^{-1}, one broad band extending from 1475 to 1555 cm^{-1} with a maximum at 1520 cm^{-1}, and a very weak peak at 1771 cm^{-1}. In addition, a sharp peak is observed at 2484 cm^{-1} with a shoulder at 2511 cm^{-1}. The intensity of all the peaks listed above decreases significantly upon in situ thermal treatment at 500 °C (Figure 4a, spectrum (2)), and becomes nearly zero after ex situ thermal treatment at 1000 °C and re-exposure to air (Figure 4a, spectrum (3)), the only exception being the peak at 1325 cm^{-1}. Finally, a peak located at ∼1710 cm^{-1} is observed in all three spectra. Peaks at {1444, 1520}, 1771, and {2484, 2511} cm^{-1} match well with the frequencies of the $\nu3$, $\nu1 + \nu4$, $\nu1 + \nu3$ modes of the CO_3^{2-} ion in bulk $SrCO_3$, respectively (see Table 2). Interestingly, however, the significant decrease

of their intensity upon in situ thermal treatment indicates that the species responsible for these bands starts to decompose below 500 °C in contrast to bulk $SrCO_3$, which decomposes above 650 °C.[23−26] Likewise, no abrupt weight loss corresponding to the decomposition of bulk $SrCO_3$ is observed above 500 °C in the thermogram corresponding to this sample (Figure 3). These observations demonstrate that the species responsible for bands at {1444, 1520}, 1771, and {2484, 2511} cm^{-1} has lower thermal stability than bulk $SrCO_3$, but the carbonate ion is in a similar crystallographic environment. Furthermore, we have observed these bands are partially restored after exposure to air for several months. On these bases, the species can be described as $SrCO_3$ located on the surface of the perovskite grains. In addition, the highly asymmetric shape of the peak at 1444 cm^{-1} suggests that other surface species, such as a strongly perturbed CO_3^{2-} ion, are also present. Finally, the peak at 1325 cm^{-1}, which does not show any significant intensity changes upon in situ and ex situ thermal treatments, arises from species with higher thermal stability than those described earlier for this sample. A similar band was observed at 1322 cm^{-1} in the DRIFT spectra of STO samples prepared by a combustion process and sintered in air for 1−96 h at temperatures between 800 and 1000 °C by Poth et al.[13] On the basis of ex situ DRIFT spectroscopy and TGA-MS data, these investigators assigned this band to a $SrCO_3$ species arising from the adsorption of CO_2 on a single SrO layer of the perovskite surface; according to their work, this species decomposes at temperatures between 200 and 500 °C. In addition, they proposed that a correlation exists between the number of SrO surface layers that incorporate atmospheric CO_2, the vibrational frequencies of the resulting $SrCO_3$ species, and their thermal stability: carbonate species closer to the surface have lower frequency and decomposition temperature. In situ DRIFT data presented here do not support these two hypotheses. In fact, the intensity of the band at 1325 cm^{-1} remains constant upon in situ thermal treatment at 500 °C, and this species has higher thermal stability than those giving rise to vibrational bands at higher frequencies. Further investigation is required to elucidate the nature and thermal stability of this species. In situ DRIFTS experiments at temperatures between 500 and 1000 °C would be useful in this regard. Finally, the peak located at ∼1710 cm^{-1} was invariably observed in all the spectra taken in the course of this work, although with variable intensity. Furthermore, it was invariably observed in the spectra of nonoxidic systems. On these bases, this band is tentatively assigned to an instrumental artifact.

The spectrum of as-prepared MSS STO nanoparticles (Figure 4b, spectrum (1)) is dominated by a broad, intense band extending from 1420 to 1570 cm^{-1}. Less intense, broad bands are observed on the low- and high-frequency sides of this main spectral feature; these are the following: a band between 1270 and 1410 cm^{-1}, which includes two weak and sharp peaks at 1383 and 1399 cm^{-1}, and a band extending from 1580 to 1720 cm^{-1}. Sharp peaks are also observed at 1770, 2484, and 2512 cm^{-1}, along with a broad shoulder at ∼2590 cm^{-1}. In situ thermal treatment causes no significant spectral changes (see Figure 4b, spectrum (2)). In contrast, ex situ thermal treatment and subsequent re-exposure to air cause the complete removal of the bands at 1420−1570, 1770, 2484, 2512, and 2590 cm^{-1}, leaving a broad band between 1270 and 1710 cm^{-1} with maxima at 1325 and a shoulder at 1380 cm^{-1} (Figure 4b, spectrum (3)). Bands at ∼1400−1600, 1770, and {2484, 2512} cm^{-1} match well with the frequencies of the $\nu 3$, $\nu 1 + \nu 4$, and $\nu 1 + \nu 3$ modes of the CO_3^{2-} ion in bulk $SrCO_3$, respectively (see Table 2); the peak at ∼2590 cm^{-1} in turn was observed in bulk $SrCO_3$ by Böttcher et al. and attributed to a combination of lattice and internal carbonate modes.[48] This assignment is further supported by XRD and TGA data reported earlier in this work, which showed the presence of ∼0.6% (w/w) bulk $SrCO_3$ in this sample. In particular, thermogravimetric data showed this phase decomposes between 680 and 800 °C (see Figure 3) in agreement with DRIFTS data. The presence of several families of surface carbonate species can be inferred from the bands at 1270−1410 and 1580−1720 cm^{-1}. These species are thermally stable up to 500 °C as none of the bands associated with them shows a significant reduction in their intensity upon in situ thermal treatment; the slight decrease in the absorbance observed in the 1600−1700 cm^{-1} region is due to the dehydration of the perovskite surface. In situ DRIFTS experiments between 500 and 1000 °C would be useful to assess the thermal stability of these surface carbonate species and, in particular, to determine whether the weak broad band extending from 1400 to 1720 cm^{-1} observed after ex situ thermal treatment, arises from their transformation upon heating or from readsorption of CO_2 upon re-exposure to air, that is, recarbonation. Finally, the band extending from 1270 to 1410 cm^{-1} with a maximum at 1327 cm^{-1} shows very little change upon in situ and ex situ thermal treatment; only the weak peaks at 1383 and 1399 cm^{-1} disappear, yielding a shoulder at 1380 cm^{-1}. As in the case of the band at 1325 cm^{-1} observed in SSR STO, further in situ spectroscopic experiments between 500 and 1000 °C are required to conclusively assign these bands.

The spectrum of as-prepared HTS STO nanoparticles (Figure 4c, spectrum (1)) exhibits a broad band extending from 1260 to 1800 cm^{-1} with local maxima at ∼1350, 1415, 1557, 1630, and 1770 cm^{-1}; in addition, a weak peak is observed at ∼2480 cm^{-1}. Thermal treatment at 500 °C causes an increase in intensity in the 1450−1500 cm^{-1} region, yielding a broad band extending from 1260 to 1600 cm^{-1} with a maximum at 1415 cm^{-1} and a weak shoulder at 1535 cm^{-1} (Figure 4c, spectrum (2)). In addition, the intensity of the band extending from 1600 to 1670 cm^{-1} decreases relative to that at 1260−1600 cm^{-1}, leaving a peak at 1630 cm^{-1} clearly observable. This peak corresponds to the bending mode of H_2O, and its presence shows that bulk dehydration is not completed at 500 °C; temperatures above 700 °C are required to achieve complete dehydration.[16,27−34,52] Peaks at 2481, 2511, and 2587 cm^{-1} also become observable after pretreatment. Finally, ex situ thermal treatment and subsequent re-exposure to air yields a broad band extending from 1260 to 1600 cm^{-1} with local maxima at ∼1331, 1390, 1449, and 1494 cm^{-1}, and a set of weak bands extending from 1630 to 1670 cm^{-1} and from 2400 to 2600 cm^{-1} (Figure 4c, spectrum (3)). On the basis of the spectral features described above, both bulk and surface carbonate species can be identified. A bulk $SrCO_3$ species gives rise to the bands at ∼1770 and ∼2491 cm^{-1} in the spectrum of as-prepared HTS STO and to the bands at 2481, 2511, and 2587 cm^{-1} observed in the spectrum of the pretreated sample. In addition, the components of the $\nu 3$ mode of the carbonate ion in this species are also certainly contributing with two bands in the 1440−1550 cm^{-1} region. The presence of bulk $SrCO_3$ is further supported by TGA data reported earlier in this work, which showed this STO sample contains ∼0.4% (w/w) of the carbonate phase. Interestingly, although TGA data showed this phase fully decomposes between 670 and 800 °C, bands at ∼1770 and ∼2492 cm^{-1} are still observable after ex situ thermal treatment at 1000 °C and subsequent re-exposure to air, demonstrating the presence of bulk $SrCO_3$. This species can be accounted for by readsorption of CO_2 on SrO layers that takes place upon re-exposure to air,

yielding $SrCO_3$ particles on the surface of the perovskite grains; the presence of a more stable form of $SrCO_3$ trapped within the bulk of the perovskite particles was ruled out on the basis of acid wash treatments. In addition to bulk $SrCO_3$ species, several families of surface carbonate species are present in the as-prepared and thermally treated HTS STO nanoparticles, demonstrating the heterogeneity of the surface for chemisorption of CO_2. These species may include symmetrical, monodentate, bidentate, and bicarbonate species (see Table 2), as well as polydentate[40] and carboxylate-like[44] structures. Although spectral ranges for the components of the $\nu 3$ mode of the carbonate ion in different configurations are available in the literature, an accurate molecular level description of the spectral features observed in Figure 4a−c requires calculation of the vibrational frequencies for CO_2 adsorbed on the SrO- and TiO_x-terminated (100) crystal plane of STO. To provide input for such theoretical work, fittings of the DRIFT spectra shown in Figure 4c were attempted; the corresponding results, as well as the details of the fitting procedure, are given in the Supporting Information. Depending on the sample treatment, a total of 16−18 local maxima were identified. Interestingly, the peak center positions remained reasonably constant upon in situ and ex situ thermal treatment; only significant changes in their relative intensities were observed, showing an interconversion process between carbonate species takes place upon changing the sample thermal treatment.

Finally, the spectrum of as-prepared TiO_2 shows very little, if any, carbonate species (Figure 4d); the weak band observed at 1644 cm^{-1} is likely due to the presence of physisorbed H_2O.

The major conclusions that emerge upon comparison of the nature of the surface carbonate species present in the as-prepared STO samples are the following: (1) The ability to reactively adsorb atmospheric CO_2 is significantly enhanced on going from TiO_2 to STO. This demonstrates that incorporation of the weakly acidic Sr^{2+} cation leads to a remarkable increase in surface basicity via exposure of highly basic SrO layers, in agreement with previous investigations of the surface acidity of STO.[4,12,13] Similarly, surface acidity studies of BTO[52] and other perovskite-type materials such as $SrZrO_3$[53] reported the preferential exposure of the alkaline-earth cation. (2) Although the presence of surface carbonate species demonstrates the existence of isolated undercoordinated metal cations and oxide anions, as well as metal cation-oxide anion acid−base pairs in the as-prepared surfaces of all three STO samples, their typology becomes increasingly complex on going from SSR to MSS and finally to HTS STO. The presence of surface carbonate species in which the carbonate ion has different crystallographic environments demonstrates the surface atomic structure strongly depends on the synthetic method employed. (3) The presence of surface carbonate species in HTS STO after ex situ thermal treatment and re-exposure to air shows that the effect of such a treatment on the surface's ability to retain or reactively readsorb CO_2 is much less significant than in the cases of SSR and MSS STO, where the quantiy of surface carbonates is much reduced after an identical treatment. Investigation of the effect of the annealing conditions, such as temperature and gaseous atmosphere, on the surface atomic structure and acidity of these nanoparticles is ongoing. (4) Finally, in the perspective of pyridine chemisorption studies it is important to mention that the presence of surface carbonate species, which are only partially removed by pretreatment, will likely prevent Lewis acidic centers involved in those species from being probed by pyridine. Complete removal of surface carbonates requires longer annealing times and higher temperatures than those employed in this work.[12,13,35,52,53] Such conditions, however, would promote significant changes in the surface morphology and atomic structure of the as-prepared surfaces, whose assessment is the objective of the present work.

TABLE 3: Frequencies (in cm^{-1}) of Relevant Fundamentals of Pyridine[a]

fundamental number[b]	vapor	liquid
ν(C═C)		
1 (A_1)	991.4	991.1
12 (A_1)	1031.6	1030.6
19b (B_2)	1441.9	1437.8
19a (A_1)	1483.4	1482.3
8b (B_2)	1580.5	1573.1
8a (A_1)	1590	1588
ν(C−H)		
20a (A_1)	3030.1	3021
7b (B_2)	3042.4	3035
13 (A_1)	3067.2	3056
20b (B_2)	3086.9	3079
2 (A_1)	3094.2	3090

[a] Data from ref 58. [b] Vibrational modes are labeled according to Wilson's notation. Symmetry species are given in parentheses.

3.2.2. Pyridine Chemisorption. The surface acidity of STO samples was assessed by means of pyridine chemisorption followed by Raman and DRIFT spectroscopy; TiO_2 anatase was used as a reference in these studies. Pyridine is a basic molecule that has been extensively used to probe the presence and nature of surface acid sites in metal oxides. Owing to the sensitivity of its vibrational modes to the nature and strength of surface acid groups, pyridine allows Lewis and Brønsted acid sites to be probed and distinguished from each other, and the acid strength of the former to be correlated with the polarizing power of the cation.[54−57] A brief summary of the relevant vibrational modes of pyridine and their corresponding frequencies in both the vapor and liquid phase is given in Table 3.[58] Fundamental frequencies shift upward upon interaction with surface Lewis and Brønsted acid sites, the magnitude of the shift being proportional to the strength of the interaction. Owing to their higher sensitivity to the nature and strength of this interaction, modes *19a*, *19b*, *8a*, and *8b*, corresponding to the ν(C═C) ring vibrations, have been almost exclusively employed in surface acidity studies of metal oxides. However, recently Travert et al. have demonstrated that fundamentals *20a*, *7b*, *13*, *20b*, and *2*, associated with ν(C−H) vibrations, can be employed to that end as well.[59] Similar to what happens to ν(C═C) vibrations, their frequencies shift upward upon interaction with surface acid centers.[59−62] In this work, pyridine adsorption was followed in three spectral regions: 950−1100 cm^{-1} (modes *1* and *12*) by visible Raman spectroscopy, and 1400−1650 cm^{-1} (modes *19a*, *19b*, *8a*, and *8b*) and 2950−3200 cm^{-1} (modes *20a*, *7b*, *13*, *20b*, and *2*) by DRIFT spectroscopy.

The Raman spectrum of pyridine chemisorbed on as-prepared TiO_2 is shown in Figure 5. It displays peaks at 993 and 1011 cm^{-1} corresponding to mode *1* and 1031 and 1042 cm^{-1} corresponding to mode *12*. Heating at 100 °C for 1 h leads to a significant decrease of the intensity of the bands at 993 and 1031 cm^{-1}, allowing the peak at 1042 cm^{-1} to be clearly observed. In situ thermal treatment at higher temperatures resulted in a strong fluorescence signal. Identical pyridine adsorption experiments were performed employing in situ pretreated TiO_2, but no differences were observed in the resulting adsorption pattern.

DRIFT spectra of pyridine chemisorbed on as-prepared and pretreated TiO_2 in the ν(C═C) region are shown in Figure 6a.

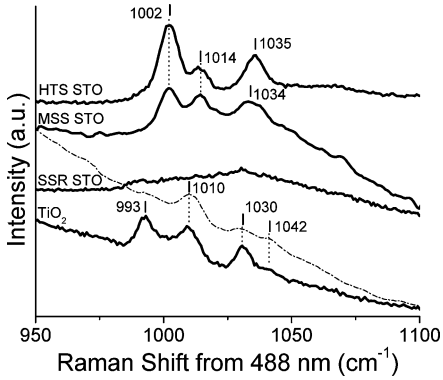

Figure 5. Raman spectra of as-prepared TiO_2, SSR, MSS, and HTS STO after pyridine chemisorption. The dashed-dotted line depicts the spectrum of TiO_2 after pyridine chemisorption and subsequent in situ thermal treatment at 100 °C for 1 h under He flow. All spectra were collected under He flow.

Py/as-prepared/TiO_2 (spectrum (1)) displays peaks at 1443, 1488, and 1575 cm^{-1}, corresponding to vibrations *19b*, *19a*, and *8b*, respectively, and at 1590, 1597, and 1604 cm^{-1}, corresponding to vibration *8a*. Py/pretreated/TiO_2 (spectrum (2)) displays similar spectral features, except for a slight upward shift of the *19b*, *19a*, and *8a* vibrations to 1444, 1489, and 1606 cm^{-1}, respectively. In addition, the band at 1597 cm^{-1} is no longer observed. Thermal treatment at 150 °C for 1 h causes further upward shift of the *19b* and *19a* vibrations to 1445 and 1491 cm^{-1}, respectively, as well as a decrease of their intensity relative to the band at 1606 cm^{-1} (spectrum (3)). In addition, the band at 1590 cm^{-1} is no longer observed. Heating at 300 °C for 1 h causes no qualitative spectral changes (spectrum (4)); however, a significant decrease in the intensity of all bands is observed, indicating the partial desorption of pyridine. Our findings are in good agreement with those reported in previous investigations of pyridine adsorption on TiO_2.[12,63−68] On this basis, bands at 1010, 1042, 1443−1445, 1488−1491, 1575, and 1604−1606 cm^{-1} are assigned to pyridine coordinated to an unsaturated Ti^{4+} cation. The peak at 1597 cm^{-1} in turn is assigned to hydrogen-bonded pyridine; clearly the surface OH groups responsible for this interaction are removed by pretreatment. Likewise, the slight upward frequency shifts observed after thermal treatment at 150 °C result from the removal of hydrogen-bonded pyridine. Finally, bands at 993, 1030, and 1590 cm^{-1} are assigned to liquid-like pyridine; the intensity of these peaks, as well as that of the peak at 1597 cm^{-1}, was found to decrease upon increasing the inert purging time, in agreement with previous investigations.[54,65]

DRIFT spectra of pyridine chemisorbed on as-prepared and pretreated TiO_2 in the ν(C−H) region are shown in Figure 6b. Py/as-prepared/TiO_2 (spectrum (1)) exhibits an intense and broad peak at 3067 cm^{-1} with a shoulder on the high frequency side, as well as weak peaks at 2998 and 3151 cm^{-1}. Similar features are displayed by Py/pretreated/TiO_2 (spectrum (2)) except for a better resolved central band, which clearly splits into two bands at 3065 and 3082 cm^{-1}. Heating at 150 °C for 1 h causes a decrease in the intensity of former relative to that of the latter, yielding two well-resolved peaks (spectrum (3)). Heating at 300 °C for 1 h causes a significant decrease in the intensity of all bands (spectrum (4)), indicating the partial desorption of chemisorbed pyridine. The spectral features observed in this region can be correlated with those observed in the ν(C═C) region. In particular, the fact that most of the hydrogen-bonded pyridine is removed after in situ thermal treatment at 150 °C, allows us to safely assume that bands observed in Py/150 °C/TiO_2 arise exclusively from the interaction of pyridine with coordinatively unsaturated Ti^{4+} cations. The doublet observed at 3065 and 3082 cm^{-1}, is directly comparable to that reported by Travert et al.[59] for pyridine chemisorbed on ZrO_2, which showed maxima at 3057 and 3074 cm^{-1}. These investigators assigned these bands to two fundamentals of pyridine coordinated to Zr^{4+}. A similar assignment is proposed for the bands at 3065 and 3082 cm^{-1} observed in this work. The larger frequency shift of the doublet at {3065, 3082} cm^{-1} relative to that at {3057, 3074} cm^{-1} doublet, reflects the higher polarizing power of the Ti^{4+} cation.[56] Assignment of these bands to a specific pair of fundamentals is, however, complicated by the presence of Fermi resonances between fundamentals and combination modes which affect both the frequencies and intensities of the resulting bands.[58,59] Indeed, one overtone and four combination modes having the same symmetry as ν(C−H) fundamentals have been observed in the spectra of vapor and liquid pyridine in the 3000−3150 cm^{-1} region; these are $\nu 8b + \nu 19b$ (A_1), $\nu 8a + \nu 19b$ (B_2), $\nu 8b + \nu 19a$ (B_2), $\nu 8a + \nu 19a$ (A_1), and $2\nu 8b$ (A_1).[58] On the basis of the previous assignments of Klots[58] and Travert et al.,[59] peaks at ∼3000 and 3150 cm^{-1} are assigned to the $\nu 8b + \nu 19b$ combination and $2\nu 8b$ overtone, respectively.

Raman spectra of pyridine chemisorbed on as-prepared SSR, MSS, and HTS STO are depicted in Figure 5. The spectra of MSS and HTS STO display peaks at 1002 and 1014 cm^{-1} corresponding to vibration *1*, and ∼1035 cm^{-1} corresponding to vibration *12*. It is worth noticing that the intensity of the band at 1014 cm^{-1} relative to that at 1002 cm^{-1} is higher in the spectrum of MSS STO than in that of HTS STO. In the case of SSR STO, the absence of observable bands belonging to chemisorbed pyridine reflects the low surface area of the microcrystalline grains. Identical experiments were performed employing in situ pretreated STO samples, but no differences were observed in the pyridine adsorption pattern.

DRIFT spectra of pyridine chemisorbed on as-prepared and pretreated SSR, MSS, and HTS STO samples in the ν(C═C) region are shown in Figure 6c,e,g, respectively. Py/as-prepared/SSR, MSS, and HTS STO (spectra (1)) display bands at 1442−1443, 1488, and 1575−1576 cm^{-1} corresponding to vibrations *19b*, *19a*, and *8b*, respectively, and at 1596−1597 and 1605−1606 cm^{-1} corresponding to vibration *8a*. Interestingly, the intensity of the band at 1605 cm^{-1} relative to that at 1597 cm^{-1} is significantly higher in the case of MSS STO than in the cases of SSR and HTS STO, where it appears as a shoulder. In addition, a weak peak corresponding to the $\nu 1 + \nu 6a$ combination is observed at 1620−1622 cm^{-1}. Py/pretreated/SSR, MSS, and HTS STO (spectra (2)) display very similar bands, except for a 1−2 cm^{-1} upward shift of some of the bands in the spectra of SSR and HTS STO. In the case of MSS STO, the band at 1605 cm^{-1} now appears as a shoulder of the band at 1597 cm^{-1}, similar to what is observed for SSR and HTS STO. Thermal treatment at 150 °C for 1 h causes further upward shift (∼1−2 cm^{-1}) of some of the bands (spectra (3)). Additionally, a decrease in the intensity of the band at 1597−1599 cm^{-1} relative to that at 1605−1606 cm^{-1} is observed in the spectra corresponding to SSR and HTS STO. Thermal treatment at 300 °C for 1 h resulted in the degradation of the signal-to-noise ratio that prevented collection of spectra in this region, except in the case of SSR STO (Figure 6c, spectrum (4)). For this sample, a significant decrease of the intensity of the band at 1599 cm^{-1} relative to that at 1606 cm^{-1} is observed. Finally, it is worth noticing that the intensity of the vibrational band corresponding to the *19b* mode relative to

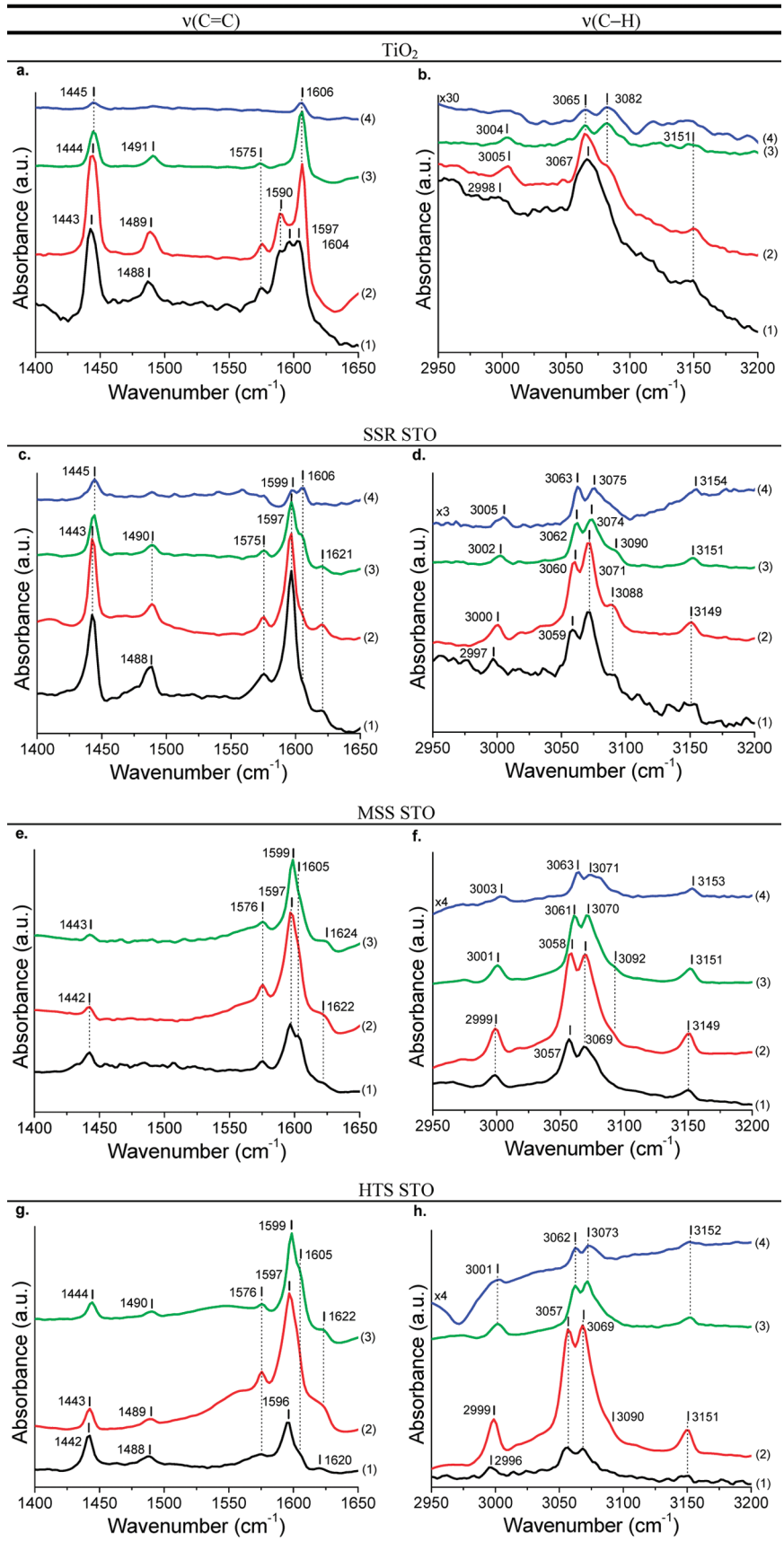

Figure 6. DRIFT spectra of pyridine chemisorbed on TiO_2, SSR STO, MSS STO, and HTS STO. Panels a, c, e, and g, and b, d, f, and h depict spectra in the regions corresponding to the ν(C═C) and ν(C−H) vibrations of pyridine, respectively. Pyridine adsorption patterns are shown in both regions for samples: (1) as-prepared (Py/as-prepared/sample), (2) pretreated (Py/pretreated/sample), (3) in situ thermally treated at 150 °C for 1 h under N_2 flow after pretreatment (Py/150 °C/sample), and (4) in situ thermally treated at 300 °C for 1 h under N_2 flow after pretreatment and in situ thermal treatment at 150 °C (Py/300 °C/sample). Spectra were collected after loading the sample in the DRIFT environmental cell, running the corresponding thermal treatment(s), and purging for 0.5 h with a high purity, dry N_2 flow.

that of the *8a* mode is significantly lower in the spectra of MSS STO and pretreated HTS STO than in those of TiO_2 and SSR STO samples. Comparison with the Raman and DRIFT spectra of pyridine chemisorbed on TiO_2 shows that the introduction of Sr^{2+} into the structure of TiO_2 leads to the splitting of vibrations *1* and *8a* into two components at 1002 and 1014 cm^{-1}, and 1597−1599 and 1605−1606 cm^{-1}, respectively, indicating the presence of two distinct surface acid sites. Earlier investigations of surface Lewis acidity of polycrystalline STO[4,12,13] and BTO[52] samples reported the presence of bands at 1001 and 1592−1597 cm^{-1} that they assigned to the *1* and *8a* modes of pyridine coordinated to the alkaline earth cation. Interestingly, only Daturi et al. reported the presence of a weak shoulder at 1606 cm^{-1} for pyridine adsorbed on STO; these authors assigned this shoulder to the *8a* mode of pyridine coordinated to a Ti^{4+} cation.[4] On this basis, peaks at 1002, 1035, and 1597−1599 cm^{-1} are assigned to the coordination of pyridine to a Sr^{2+} cation (Py/Sr^{2+}), whereas those at 1014 and 1605−1606 cm^{-1} are assigned to the coordination of pyridine to a Ti^{4+} cation (Py/Ti^{4+}). The acid strength of each of these sites is further confirmed by in situ thermal treatment at 150 and 300 °C, which cause a decrease in the intensity of the band at 1597−1599 cm^{-1} relative to that at 1605−1606 cm^{-1}. Interesting is the case of MSS STO, for which the ratio of Ti^{4+} to Sr^{2+} sites probed by pyridine in the as-prepared surfaces appears to be slightly higher than in SSR and HTS STO samples. Because all three pretreated STO samples display very similar pyridine chemisorption patterns, and since no significant changes in the nature of carbonate species are observed upon pretreatment of MSS STO (Figure 4b), this observation can be rationalized by invoking a higher degree of hydroxylation of the Sr^{2+} sites on as-prepared MSS STO, which prevents them from being probed by pyridine. Finally, it should be noticed that modes *19a*, *19b*, and *8b* are less sensitive to the acid strength of the metal cations than vibrations *1*, *12*, and *8a*, as indicated by the much smaller upward shifts observed upon coordination. Frequency shifts reported herein for these vibrations are in good agreement with those reported in previous investigations of pyridine chemisorption on STO[4,12,13] and BTO.[52]

DRIFT spectra of pyridine chemisorbed on as-prepared and pretreated SSR, MSS, and HTS STO samples in the ν(C−H) region are shown in Figure 6d,f,h, respectively. Py/as-prepared/SSR, MSS, and HTS STO (spectra (1)) are dominated by an intense band in the 3050−3100 cm^{-1} region consisting of a pair of peaks at {3059, 3071} cm^{-1} in the case SSR STO and {3057, 3069} cm^{-1} in the cases of MSS and HTS STO. Two weak peaks at 2996−2999 and 3149−3151 cm^{-1} are also observed in all three spectra. In addition, a peak at 3088 cm^{-1} is clearly observed in the case of SSR STO. Py/pretreated/SSR, MSS, and HTS STO (spectra (2)) display similar features, the only differences being a slight upward shift of the weak peak at ∼3000 cm^{-1}, and the appearance of a weak shoulder at 3090−3092 cm^{-1} in the spectra of MSS and HTS STO. Heating at 150 °C for 1 h causes further upward shift of all bands (spectra (3)), including the central pair of peaks, which is now located at {3062, 3074}, {3061, 3070}, and {3062, 3073} cm^{-1} in the cases of SSR, MSS, and HTS STO, respectively. Unlike the ν(C═C) region, collection of spectra after in situ thermal treatment at 300 °C for 1 h was possible in the ν(C−H) region (spectra (4)). No qualitative changes are observed for all three STO samples, except for a significant decrease in the intensity of all bands, indicating the partial desorption of chemisorbed pyridine. Although the weak peak at ∼3090 cm^{-1} is no longer observed in these spectra, the asymmetry of the high frequency side of the central band is still noticeable. Similar to the analysis of the spectra of pyridine chemisorbed on TiO_2 in the ν(C−H) region, it is assumed that the bands observed in the spectra of pyridine chemisorbed on STO samples after thermal treatment at 150 °C arise exclusively from the coordination of pyridine to metal cations. Comparison of the spectra of Py/150 °C/SSR, MSS, and HTS STO with that of Py/150 °C/TiO_2, shows that the central pair of peaks appears at wavenumbers systematically lower in the case of STO samples, {3061−3063, 3071−3074} cm^{-1} in the former versus {3065, 3082} cm^{-1} in the latter. This is reflecting the lower polarizing power of the metal cations to which pyridine is coordinated to in the case of STO samples. On this basis and taking into account the predominance of Sr^{2+} sites observed in the ν(C═C) region, the doublet at {3061−3063, 3071−3074} cm^{-1} is assigned to two fundamentals of pyridine coordinated to Sr^{2+}. The weak peak at ∼3090 cm^{-1} in turn could belong either to a third fundamental of pyridine or to a combination mode. Chemisorption experiments with deuterated pyridine would facilitate a more conclusive assignment of this band and clarification of the contribution of combination modes to the spectral features observed in this region. Finally, similar to the case of pyridine chemisorbed on TiO_2 peaks at ∼3000 and 3150 cm^{-1} are assigned to the $\nu 8b + \nu 19b$ combination mode and the $2\nu 8b$ overtone, respectively.

Raman and DRIFT spectra of pyridine chemisorbed on STO samples demonstrate the weak Lewis acid character of these surfaces, as well as the absence of Brønsted acid sites strong enough to protonate pyridine. It is clear from chemisorption of pyridine that the differences in surface acidity are rather slight, the surface of STO grains consisting of a mixture of SrO-based and TiO-based terminations, regardless of the synthetic approach employed in their preparation. Although overlooked in previous investigations, the presence of coordinatively unsaturated Ti^{4+} centers reported in this work deserves particular attention since these centers will undoubtedly influence the reactivity of these surfaces. Indeed, it was reported that acid−base pairs consisting of a high valency transition metal cation and a highly nucleophilic oxide anion are involved in the activation and heterolytic dissociation of C−H bonds during the partial and total oxidation of hydrocarbons over perovskite-type materials.[3,4,69] Although the magnitude of the shifts of the vibrational bands of pyridine observed upon adsorption are very similar for all three STO samples, the relative IR activities of bands *19b* and *8a* change significantly upon going from irregularly shaped grains to cubic-shaped, (100)-oriented nanoparticles. The IR activity of the vibrational modes of adsorbed pyridine is determined by the orientation of the molecule with respect to the surface, which is in turn dependent on the surface nature, coverage, and temperature.[70] Changes observed in the relative IR activities of modes *19b* and *8a* observed for a given sample upon variation of the thermal treatment conditions can be ascribed to a change in the adsorption geometry of pyridine induced by a change in the surface coverage. Changes in the relative intensities of these two bands observed upon going from SSR STO to MSS and HTS STO indicate that the adsorption geometry of pyridine is different for cubic-shaped, (100)-oriented nanoparticles. The coupling of the dynamic dipole of the vibrational modes to the corresponding induced surface image dipole might be influencing their relative activities as well.[70,71] Further investigation is required to clarify the features of the nanoparticles's surface that cause such a distinct intensity pattern.

From the perspective of using size- and shape-controlled STO nanoparticles as supports for such catalytic applications, possessing a quantitative estimate of the surface acid sites available

for reaction under a given set of experimental conditions is as important as knowing the chemical nature of these sites. Owing to their higher surface area and uniform and regular cubic shape, HTS STO nanocubes were employed as substrates in quantitative studies of surface Lewis acidity. To this end, the adsorption of pyridine and ammonia was followed gravimetrically. The election of these molecular probes was based on their significantly different kinetic diameters: 0.585 nm for pyridine versus 0.165 nm for ammonia. This size difference should allow the smaller molecule to probe sites which are not accessible for the larger one, thereby revealing the presence of nanosized pores in the surface. Interestingly, the acid site coverages obtained with both molecules were very similar, in the range 6.5−13 μmol/g STO, which is equivalent to 0.2−0.4 molecules/nm^2. The surface density was computed from the BET surface area of as-prepared HTS STO nanoparticles, which did not show any significant change after pretreatment. The very similar results obtained with pyridine and ammonia, indicate that the Lewis acid centers in the surface are equally accessible to both bases; no sterically restricted Lewis acid sites were detected, showing the presence of nanosized pores at the surface is negligible. In addition, it is worth pointing out that, although the molecules might be probing Sr^{2+} sites located in $SrCO_3$ surface layers that are not removed by pretreatment, the total Lewis surface acidity given above represents an estimate of the actual number of surface Lewis acid sites available for reaction under the experimental conditions employed in this work.

4. Conclusions

A comparative study of the surface acidity and structure of as-prepared polycrystalline STO samples synthesized using three different approaches was carried out by means of pyridine and atmospheric CO_2 adsorption followed by visible Raman and DRIFT spectroscopy. Chemisorption of both molecular probes demonstrated that the differences in surface acidity between samples synthesized using different approaches are rather slight with a mixture of SrO-based and TiO-based terminations observed in all cases. However, the typology of surface carbonate species arising from the reactive adsorption of atmospheric CO_2 varied significantly between samples, indicating the surface atomic structure of as-prepared and thermally treated STO surfaces depend strongly on the synthetic method employed.

Interestingly, from the perspective of employing size- and shape-controlled STO nanoparticles as supports in catalytic applications is the case of STO nanocubes synthesized via sol-precipitation-hydrothermal treatment. In addition to their single-crystalline character, negligible porosity, and well-defined {100} flat faces, these nanoparticles exhibit coordinatively unsaturated Ti^{4+} and highly nucleophilic O^{2-} surface centers. These features are relevant for the activation of C−H bonds required for the oxidation of hydrocarbons. XPS experiments that give further insight into the surface composition and crystallographic environment of the Lewis acid centers present in these nanocubes would be worthwhile to establish surface structure-surface chemistry relationships for selected hydrocarbon oxidation reactions.

Acknowledgment. This work was supported by the Chemical Sciences, Geosciences, and Biosciences Division, Office of Basic Energy Sciences, Office of Science, U.S. Department of Energy (Award No. DE-FG02-03-ER15457).

This work made use of J. B. Cohen X-ray Diffraction Facility supported by the MRSEC program of the National Science Foundation (DMR-0520513) at the Materials Research Center of Northwestern University.

The DRIFTS work was performed in the Keck-II facility of NUANCE Center at Northwestern University. NUANCE Center is supported by NSF-NSEC, NSF-MRSEC, Keck Foundation, the State of Illinois, and Northwestern University.

The authors are grateful to Dr. Jeffrey W. Elam from Argonne National Laboratory for providing the scanning electron microscopy picture shown in the Table of Contents.

Supporting Information Available: DRIFT spectra of as-prepared and thermally treated HTS STO nanoparticles in the ν(O−H) region, and fittings of DRIFT spectra of as-prepared and thermally treated HTS STO nanoparticles in the 1250−1800 cm^{-1} region. This material is available free of charge via the Internet at http://pubs.acs.org.

References and Notes

(1) Vendik, O. G.; Hollmann, E. K.; Kozyrev, A. B.; Prudan, A. M. *J. Supercond.* **1999**, *12*, 325–338.
(2) Xi, X. X.; Li, H. C.; Si, W. D.; Sirenko, A. A.; Akimov, I. A.; Fox, J. R.; Clark, A. M.; Hao, J. H. *J. Electroceram.* **2000**, *4*, 393–405.
(3) Ding, W.; Chen, Y.; Fu, X. *Appl.Catal., A* **1993**, *104*, 61–75.
(4) Daturi, M.; Busca, G.; Groppi, G.; Forzatti, P. *Appl. Catal., B* **1997**, *12*, 325–337.
(5) Wrighton, M. S.; Ellis, A. B.; Wolczanski, P. T.; Morse, D. L.; Abrahamson, H. B.; Ginley, D. S. *J. Am. Chem. Soc.* **1976**, *98*, 2774–2779.
(6) Wagner, F. T.; Somorjai, G. A. *Nature* **1980**, *285*, 559–560.
(7) Wagner, F. T.; Somorjai, G. A. *J. Am. Chem. Soc.* **1980**, *102*, 5494–5502.
(8) Avudaithai, M.; Kutty, T. R. N. *Mater. Res. Bull.* **1987**, *22*, 641–650.
(9) Hemminger, J. C.; Carr, R.; Somorjai, G. A. *Chem. Phys. Lett.* **1978**, *57*, 100–104.
(10) Aurian-Blajeni, B.; Halmann, M.; Manassen, J. *Solar Energy* **1980**, *25*, 165–170.
(11) Tinnemans, A. H. A.; Koster, T. P. M.; Thewissen, D.; Mackor, A. *New J. Chem.* **1982**, *6*, 373–379.
(12) Gallardo Amores, J. M.; Escribano, V. S.; Daturi, M.; Busca, G. *J. Mater. Chem.* **1996**, *6*, 879–886.
(13) Poth, J.; Haberkorn, R.; Beck, H. P. *J. Eur. Ceram. Soc.* **2000**, *20*, 715–723.
(14) Rabuffetti, F. A.; Kim, H. S.; Enterkin, J. A.; Wang, Y. M.; Lanier, C. H.; Marks, L. D.; Poeppelmeier, K. R.; Stair, P. C. *Chem. Mater.* **2008**, *20*, 5628–5635.
(15) Chua, Y. T.; Stair, P. C. *J. Catal.* **2000**, *196*, 66–72.
(16) Hennings, D.; Schreinemacher, S. *J. Eur. Ceram. Soc.* **1992**, *9*, 41–46.
(17) Balaya, P.; Ahrens, M.; Kienle, L.; Maier, J.; Rahmati, B.; Lee, S. B.; Sigle, W. *J. Am. Ceram. Soc.* **2006**, *89*, 2804–2811.
(18) Perry, C. H.; Fertel, J. H.; McNelly, T. D. *J. Chem. Phys.* **1967**, *47*, 1619–1625.
(19) Nilsen, W. G.; Skinner, J. G. *J. Chem. Phys.* **1968**, *48*, 2240–2248.
(20) Balachandran, U.; Eror, N. G. *J. Am. Ceram. Soc.* **1982**, *65*, C54–C56.
(21) Ohsaka, T.; Izumi, F.; Fujiki, Y. *J. Raman Spectrosc.* **1978**, *7*, 321–324.
(22) Balachandran, U.; Eror, N. G. *J. Solid State Chem.* **1982**, *42*, 276–282.
(23) Judd, M. D.; Pope, M. I. *J. Therm. Anal.* **1972**, *4*, 31–38.
(24) Koga, N.; Tanaka, H. *J. Therm. Anal.* **1988**, *34*, 177–188.
(25) Arvanitidis, I.; Sichen, D.; Sohn, H. Y.; Seetharaman, S. *Metall. Mater. Trans. B* **1997**, *28B*, 1063–1068.
(26) L'vov, B. V.; Ugolkov, L. *Thermochim. Acta* **2004**, *409*, 13–18.
(27) Vivekanandan, R.; Philip, S.; Kutty, T. R. N. *Mater. Res. Bull.* **1987**, *22*, 99–108.
(28) Yen, F.-S.; Hsiang, H.-I.; Chang, Y.-W. *Jpn. J. Appl. Phys., Part 1* **1995**, *34*, 6149–6155.
(29) Wada, S.; Suzuki, T.; Tatsuo, N. *Jpn. J. Appl. Phys., Part 1* **1995**, *34*, 5368–5379.
(30) Wada, S.; Suzuki, T.; Noma, T. *J. Ceram. Soc. Jpn.* **1995**, *103*, 1220–1227.
(31) Wada, S.; Suzuki, T.; Noma, T. *J. Ceram. Soc. Jpn.* **1996**, *104*, 383–392.
(32) Noma, T.; Wada, S.; Yano, M.; Suzuki, T. *J. Appl. Phys.* **1996**, *80*, 5223–5233.
(33) Shi, E.-W.; Xia, C.-T.; Zhong, W.-Z.; Wang, B.-G.; Feng, C.-D. *J. Am. Ceram. Soc.* **1997**, *80*, 1567–1572.

(34) Clark, I. J.; Takeuchi, T.; Ohtori, N.; Sinclair, D. C. *J. Mater. Chem.* **1999**, *9*, 83–91.
(35) Munuera, G.; Gonzalez Elipe, A. R.; Espinos, J. P.; Lopez Molina, E. *Surf. Interface Anal.* **1990**, *15*, 693–697.
(36) Herard, C.; Faivre, A.; Lemaitre, J. *J. Eur. Ceram. Soc.* **1995**, *15*, 135–143.
(37) Blanco Lopez, M. d.-C.; Fourlaris, G.; Rand, B.; Riley, F. L. *J. Am. Ceram. Soc.* **1999**, *82*, 1777–1786.
(38) Viviani, M.; Buscaglia, M. T.; Nanni, P.; Parodi, R.; Gemme, G.; Dacca, A. *J. Eur. Ceram. Soc.* **1999**, *19*, 1047–1051.
(39) Hair, M. L. *Infrared Spectroscopy in Surface Chemistry*; Marcel Dekker, Inc.: New York, 1967.
(40) Busca, G.; Lorenzelli, V. *Mater. Chem.* **1982**, *7*, 89–126.
(41) Ramis, G.; Busca, G.; Lorenzelli, V. *Mater. Chem. Phys.* **1991**, *29*, 425–435.
(42) Morterra, C.; Cerrato, G.; Emanuel, C. *Mater. Chem. Phys.* **1991**, *29*, 447–456.
(43) Herzberg, G. *Infrared and Raman Specta of Polyatomic Molecules*; D. Van Nostrand: New York, 1945.
(44) Miller, F. A.; Wilkins, C. H. *Anal. Chem.* **1952**, *24*, 1253–1294.
(45) Huang, C. K.; Kerr, P. F. *Am. Mineral.* **1960**, *45*, 311–324.
(46) Adler, H. H.; Kerr, P. F. *Am. Mineral.* **1963**, *48*, 124–137.
(47) Alia, J. M.; de Mera, Y. D.; Edwards, H. G. M.; Martin, P. G.; Andres, S. L. *Spectrochim. Acta, Part A* **1997**, *53*, 2347–2362.
(48) Bottcher, M. E.; Gehlken, P. L.; Fernandez Gonzalez, A.; Prieto, M. *Eur. J. Mineral.* **1997**, *9*, 519–528.
(49) Gatehouse, B. M.; Livingstone, S. E.; Nyholm, R. S. *J. Chem. Soc.* **1958**, 3137–3142.
(50) Fujita, J.; Martell, A. E.; Nakamoto, K. *J. Chem. Phys.* **1962**, *36*, 339–335.
(51) Little, L. H. *Infrared Spectra of Adsorbed Species*; Academic Press: New York, 1966.
(52) Busca, G.; Buscaglia, V.; Leoni, M.; Nanni, P. *Chem. Mater.* **1994**, *6*, 955–961.
(53) Daturi, M.; Busca, G.; Willey, R. J. *Chem. Mater.* **1995**, *7*, 2115–2126.
(54) Kung, M. C.; Kung, H. H. *Catal. Rev.—Sci. Eng.* **1985**, *27*, 425–460.
(55) Lercher, J. A.; Grundling, C.; Eder Mirth, G. *Catal. Today* **1996**, *27*, 353–376.
(56) Busca, G. *Catal. Today* **1998**, *41*, 191–206.
(57) Busca, G. *Phys. Chem. Chem. Phys.* **1999**, *1*, 723–736.
(58) Klots, T. D. *Spectrochim. Acta, Part A* **1998**, *54*, 1481–1498.
(59) Travert, A.; Vimont, A.; Sahibed-Dine, A.; Daturi, M.; Lavalley, J. C. *Appl. Catal., A* **2006**, *307*, 98–107.
(60) Mizutani, G.; Ushioda, S. *J. Phys. Chem.* **1989**, *91*, 598–602.
(61) Wu, D.-Y.; Ren, B.; Jiang, Y.-X.; Xu, X.; Tian, Z.-Q. *J. Phys. Chem. A* **2002**, *106*, 9042–9052.
(62) Martins, J. B. L.; Fialho, T. A. S. *J. Mol. Struct.: THEOCHEM* **2005**, *732*, 1–5.
(63) Primet, M.; Pichat, P.; Mathieu, M. V. *J. Phys. Chem.* **1971**, *75*, 1221–1226.
(64) Parfitt, G. D.; Ramsboth, J; Rochester, C. H. *Trans. Faraday Soc.* **1971**, *67*, 1500–1506.
(65) Morterra, C.; Ghiotti, G.; Garrone, E.; Fisicaro, E. *J. Chem. Soc., Faraday Trans. I* **1980**, *76*, 2102–2113.
(66) Busca, G.; Saussey, H.; Saur, O.; Lavalley, J. C.; Lorenzelli, V. *Appl. Catal.* **1985**, *14*, 245–260.
(67) Dines, T. J.; Rochester, C. H.; Ward, A. M. *J. Chem. Soc., Faraday Trans.* **1991**, *87*, 643–651.
(68) Ferretto, L.; Glisenti, A. *Chem. Mater.* **2003**, *15*, 1181–1188.
(69) Burch, R.; Hayes, M. J. *J. Mol. Catal A: Chem.* **1995**, *100*, 13–33.
(70) Haq, S.; King, D. A. *J. Phys. Chem.* **1996**, *100*, 16957–16965.
(71) Pearce, H. A.; Sheppard, N. *Surf. Sci.* **1976**, *59*, 205–217.

JP101727C